Optical and Electrical Properties of Proton-Implanted *p*-GaSb for Electrical Isolation

Sk Shafaat Saud Nikor[1], Md Saiful Islam Sumon[1], Shrivatch Sankar[1], Like Ma[1], Victor J. Patel[2], Samuel D. Hawkins[2], Sadhvikas J. Addamane[3], and Shamsul Arafin[1]*

[1]*Department of Electrical and Computer Engineering, The Ohio State University, Columbus, OH 43210, USA*

[2]*Center for Integrated Nanotechnologies, Sandia National Laboratories, Albuquerque, New Mexico 87123, USA*

[3]*Sandia National Laboratories, Albuquerque, NM 87123, USA*

*E-mail: arafin.1@osu.edu

The effect of proton implantation as isolation implant and subsequent annealing on the optical absorption and electrical resistivity of low-bandgap *p*-GaSb is reported. The measured transmittance spectra indicates that implantation creates a distribution of energy levels extending into the bandgap. Electrical measurements show that the average sheet resistance of the implanted layer increases only by an order of magnitude from its pre-implantation value at a proton dose of ~10^{13} cm^{-2} followed by 200°C annealing. It is also shown that annealing reduces the implantation-induced optical absorption while still retaining a high electrical resistivity.

The extended short and mid-wave infrared (eS-MWIR) regime of the electromagnetic spectrum, covering wavelengths ranging from 2 μm to 6 μm, contains a number of spectral features such as strong overtones and combination molecular absorption bands in gas- and liquid-phase molecules. The presence of strong absorption lines for chemically and biologically important trace compounds such as water vapor, hydrogen sulfide, hydrogen cyanide, and nitrous oxide in the MWIR wavelength regime enables photonic sensors to detect these compounds with high selectivity and sensitivity [1]. This is useful for a wide range of applications including non-invasive medical diagnostics [2], industrial process control [3], and biochemical sensing [4, 5].

Photonic integrated circuits (PICs) with tightly-integrated active and passive optoelectronic components that operate in this wavelength regime have received growing research interest in recent years. PICs containing active and passive photonic components connected with low-loss passive waveguides are of utmost importance for implementing eS-MWIR photonic sensor technologies at the chip scale as integrated low-cost solutions [6]. Although MWIR PICs have recently been demonstrated using heterogeneous integration of GaSb-based interband cascade lasers (ICLs) with silicon-on-insulator passive components [7-9], device performance was limited by the challenge of bonding GaSb to silicon. A monolithic platform alleviates this problem with the tight integration of both active and passive components on the material platform based on GaSb and its alloys.

Realizing complex and monolithic PICs requires the spatially selective control of electrical properties, such as resistivity, and optical properties, such as absorption coefficient. Ion implantation is the technique of choice for selectively producing high-resistivity regions for electrical isolation between devices within a PIC [10]. Device isolation is a key processing step and is used to restrict current flow to active devices without having cross-talk with other areas on a wafer [11]. To this end, ion implantation has the obvious advantage over mesa etching that it retains the planarity of the surface and, in general, intrudes less under mask edges. Typically, light ions are used and the layer of high resistivity results from the defects created in the lattice by the ions, whereby the ion damage manifests as trap states. Antisite defects or defect-related complexes are formed by replacement collisions and act as deep-level charge carrier trapping centers that are not thermally ionized at normal operating temperatures. Although these defects are detrimental to

the optical performance of semiconductor devices, treatments such as rapid thermal annealing (RTA) essentially recover the implantation-induced optical absorption back to the pre-implantation value while still retaining a sufficiently high resistivity [12]. Optical loss is also reduced after implantation due to lower free carrier absorption since implanted ions passivate dopant sites.

Although the effects of ion implantation, including hydrogen ion (proton) implantation, have been widely investigated in material systems such as InP [13-17], GaAs [12, 18], GaP [19, 20], and InAs [20, 21], similar studies on GaSb are few and far between. There are only a few reports that discuss ion implantation in GaSb [22-26]. However, these works do not address the precise effects of proton implantation on the optical and electrical properties of GaSb, instead focusing on morphological changes such as anomalous swelling [27, 28] and porosity [29] brought about by the implantation of heavier ions. Two recent works examined the effect of proton implantation and zinc ion implantation on InAs/AlSb superlattice-based ICLs [30] and -photodetectors [31], respectively, but to the best of our knowledge a comprehensive study of proton implantation on low-bandgap materials, e.g., GaSb is still wanting.

In this study, we endeavor to find the optimal proton implantation parameters (energy and dose values) and the optimal temperature for subsequent RTA cycles which maximize the electrical resistivity of *p*-GaSb while keeping its implantation-induced optical absorption to a minimum. As a material, *p*-GaSb is experimentally investigated in this study since *p*-doped layers act as upper cladding regions of a PIC. Hence, selectively controlling its resistivity and absorption coefficient is of vital importance to the feasibility of the PIC. It is found that proton implantation at a dose of 10^{13} cm^{-2} and subsequent RTA at 200°C increases resistivity by more than one order of magnitude from its pre-implantation value while significantly reducing implantation-induced optical absorption.

The two types of samples used in this study are schematically shown in **Figs. 1(a) and 1(b)**. *p*-GaSb wafers with a carrier concentration of 1×10^{18} cm^{-3} were used for pre- and post-implantation optical characterization. 1 cm×1 cm samples were cleaved from the wafer and implanted with protons of multiple energies and doses. **Table I** outlines these parameters, with energies varying over the range 20–175 keV and doses varying over the range 10^{10}–10^{15} cm^{-2}.

Table I. Proton energy and dose combinations explored in this study.

Energy and dose combinations			
A	B	C	D
175 keV @ 9×10^{10} cm^{-2}	175 keV @ 9×10^{12} cm^{-2}	175 keV @ 9×10^{13} cm^{-2}	175 keV @ 9×10^{15} cm^{-2}
110 keV @ 7×10^{10} cm^{-2}	110 keV @ 7×10^{12} cm^{-2}	110 keV @ 7×10^{13} cm^{-2}	110 keV @ 7×10^{15} cm^{-2}
55 keV @ 5×10^{10} cm^{-2}	55 keV @ 5×10^{12} cm^{-2}	55 keV @ 5×10^{13} cm^{-2}	55 keV @ 5×10^{15} cm^{-2}
20 keV @ 4×10^{10} cm^{-2}	20 keV @ 4×10^{12} cm^{-2}	20 keV @ 4×10^{13} cm^{-2}	20 keV @ 4×10^{15} cm^{-2}

Using Transport of Ions in Matter (TRIM) [32] simulations, these parameters were predicted to result in a proton-implanted layer of thickness 2 µm in GaSb. **Figure 1(c)** shows the spatial distribution of protons resulting from implantation as determined by TRIM simulations. All implantations were performed at room temperature in order of decreasing implant energies due to the fact that for low-energy implantations, the lateral spread of ions is far lower for decreasing energies than it is for increasing energies. The surface normal of the sample was inclined at 7° with respect to the beam to minimize ion channeling. All implants were done at an ion current density < 0.1 µA/cm². Prior to implantation, optical transmission was determined using a Fourier transform infrared (FTIR) spectrometer. The process was repeated after implantation, and after post-implantation annealing cycles were performed in nitrogen atmosphere in a RTA furnace. The samples were heated from room temperature up to the final temperature with a heating rate of 50°C/s. After the final temperature was reached it was maintained constant for 10 s.

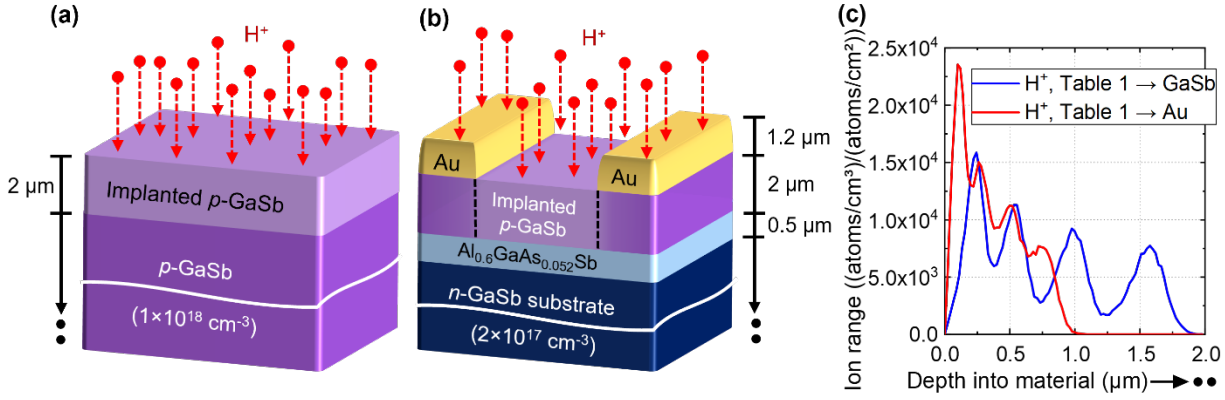

Fig. 1. Test samples used to conduct pre- and post-implantation (a) optical (blanket implantation) and (b) electrical (selective area implantation) characterization, (c) TRIM simulations for proton implantation on GaSb and Au with the parameters outlined in **Table I**.

Electrical characterization was carried out on a test structure grown by molecular beam epitaxy, as shown in **Fig. 1(b)**. The structure consists of high-bandgap quaternary lattice-matched $Al_{0.6}GaAs_{0.052}Sb$ and 2-μm-thick *p*-GaSb with the same doping concentration as in the bare wafer. Such a test structure helps obtain good current confinement within the layer under study. 1 cm^2 samples were cleaved and standard optical lithography was done to define an array of transfer length method (TLM) pads and clover-leaf Hall patterns. Ohmic contacts composed of Ti(30 nm)/Pt(30 nm)/Au(200 nm) were evaporated on each sample. Electroplating methods were then employed to bring the total gold thickness up to 1.2 μm. In this case, ohmic contacts were deposited prior to isolation implants so that they acted as a mask which prevented the implantation of the covered GaSb layer and hence introduced implantation selectivity as is desirable in an actual PIC. The minimum thickness required for this mask was determined by TRIM simulations as shown in **Fig. 1(c)**. Proton implantations were carried out on these electrical test structures as per **Table I**, this time with the objective of fully implanting the 2-μm-thick top *p*-GaSb layer.

The spatial distribution of implantation-induced defects is found to be slightly skewed towards the *p*-GaSb surface according to TRIM simulations. This nonuniform distribution implies that the optical absorption coefficient and electrical resistivity are depth dependent. The optical and electrical measurements produce average values of these quantities over the thickness of the implanted layer.

In order to characterize the optical absorption coefficient introduced by proton implantation, the transmitted light intensity was measured using FTIR spectroscopy by passing convergent light from a tungsten-halogen source through the unimplanted (i.e., bare substrates) and implanted samples, respectively. The transmitted light intensity was recorded as a function of wavelength in each case, as shown in **Fig. 2**. As expected, the transmission spectra rises abruptly at the bandgap energy of GaSb which corresponds to a wavelength of ~1.8 μm. For a given incident light intensity I_0, the transmitted light intensities at any given wavelength above ~2.1 μm, at which the transmission intensities change to a constant level, for the unimplanted and implanted samples are designated I_1 and I_2, respectively. The ratio I_2/I_1 is closely linked to the implantation-induced absorption coefficient. The transmitted light intensity through the implanted part of the sample is

$$I_2 = R \exp[-(\alpha_1 d_1 + \alpha_2 d_2)]$$

where α_1 is the absorption coefficient of the unimplanted material and α_2 is the additional

absorption coefficient introduced by the proton implantation, and d_1 and d_2 are the thicknesses of the unimplanted layer and the total sample, respectively. R is the reflectivity factor which accounts for reflection losses at both surfaces. To a good approximation the reflectivity factor may be assumed to be the same for the implanted and unimplanted parts of the sample.

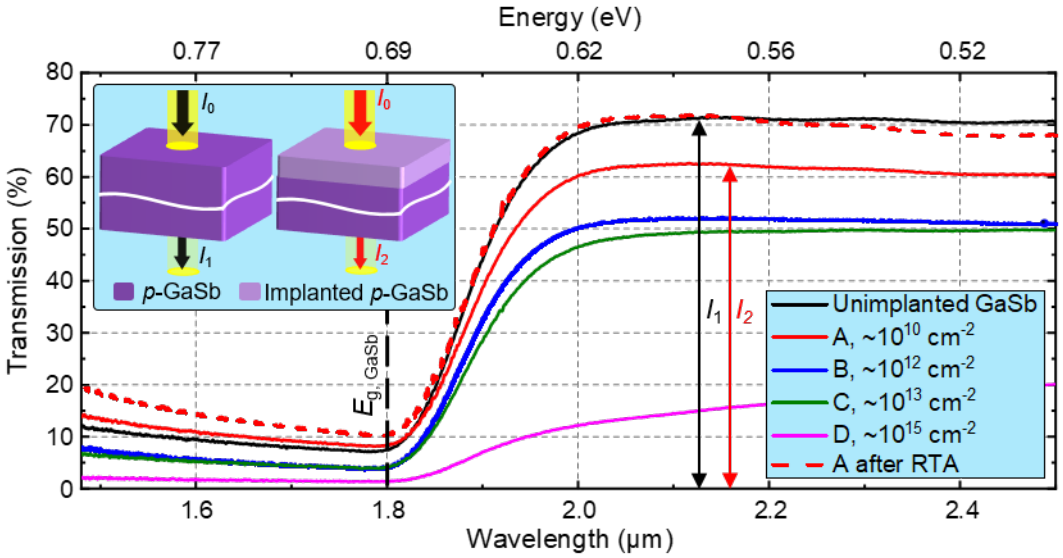

Fig. 2. Transmission of light through unimplanted and implanted *p*-GaSb samples. Solid lines show typical transmission for an unimplanted sample compared with transmission after implantation at various energies and doses. The dashed line shows how implantation-induced optical absorption is reduced after annealing at 175°C for 10 s.

Therefore,

$$\frac{I_2}{I_1} = \exp(-\alpha_2 d_2)$$

and the ratio I_2/I_1 provides a measure of the additional absorption due to the proton implantation only. Rewriting, we get

$$\alpha_2 = \frac{1}{d_2} \ln\left(\frac{I_1}{I_2}\right)$$

The ratio I_2/I_1 is thus indicative of α_2, a useful measure of the number of optically-active defects produced by implantation. **Figure 2** shows that for energy and dose combination-A (with reference to **Table I**), i.e., proton doses in the order of 10^{10} cm^{-2}, the ratio I_2/I_1 is 0.86. This indicates that 14% of the light is either absorbed or scattered by the proton-implanted layer. From similar calculations for the higher doses, it is evident that proton implantation creates a distribution of

optically absorbing energy levels which extends well into the bandgap of the material under study, and this effect increases with increasing dose. A representative optical transmittance spectrum after annealing at 175°C for 10 s is also shown in **Fig. 2**. For energy and dose combination-A, the ratio I_2/I_1 recovers to 0.96 after the annealing. With increase in annealing temperature, the transmission spectra are found to move towards and eventually converge with the unimplanted spectrum. Interestingly, the ratio I_2/I_1 exceeds unity at certain wavelengths. This implies that the reduction in free carrier absorption more than compensates for the increased absorption introduced by the damage.

Figure 3 shows the ratio I_2/I_1 following implantation and various annealing treatments as a function of proton dose. It is evident that annealing can recover the implantation-induced optical absorption, often to pre-implantation levels. For lower implantation doses, optical damage is annealed out relatively easily. Higher annealing temperatures are required to recover from higher doses. Significant annealing occurs at each higher temperature used.

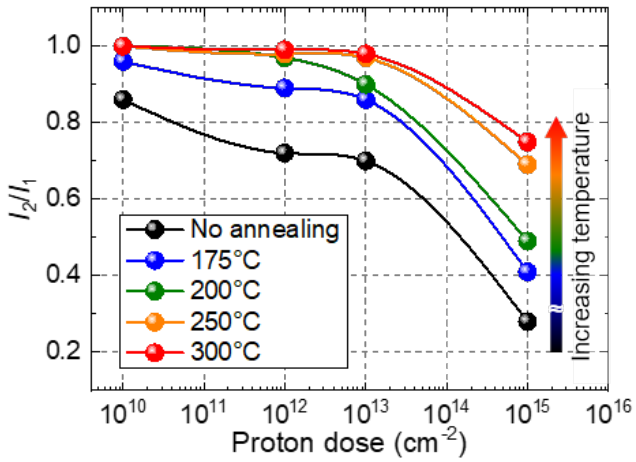

Fig. 3. The ratio I_2/I_1 as a function of proton dose for various annealing conditions applied on implanted *p*-GaSb samples. The curves show that the ratio I_2/I_1 can be recovered towards unity where the implantation-induced optical absorption has been eliminated.

The change in electrical resistivity caused by proton implantation was then analyzed. The magnitudes of sheet resistance, which is analogous to resistivity, were obtained from the slopes of linear *I-V* plots over the range ±1 V. Sheet resistance measurements were carried out using both TLM- and Hall measurements with van der Pauw geometry. The measured results from these two

methods agree closely with each other. Energy and dose combination-A, with dose values of ~10^{10} cm^{-2}, was found not to produce any significant increase in sheet resistance. Combinations-B, -C, and -D were more effective in this regard. Combination-C, with dose values ~10^{13} cm^{-2}, has a special significance since the highest electrical resistivity occurs at this value. Ion doses higher than those in combination-D are known to produce swelling and morphological degradation in GaSb and were not explored in our study. Post-implantation RTA cycles with the aforementioned conditions were again performed and the behavior of the sample was investigated at each RTA temperature. RTA temperatures over the range 150°–375°C were employed and RTA cycles were accumulated in the samples. The average sheet resistance obtained from combination-C, determined using TLM and Hall measurements, is plotted in **Fig. 4** for various annealing conditions.

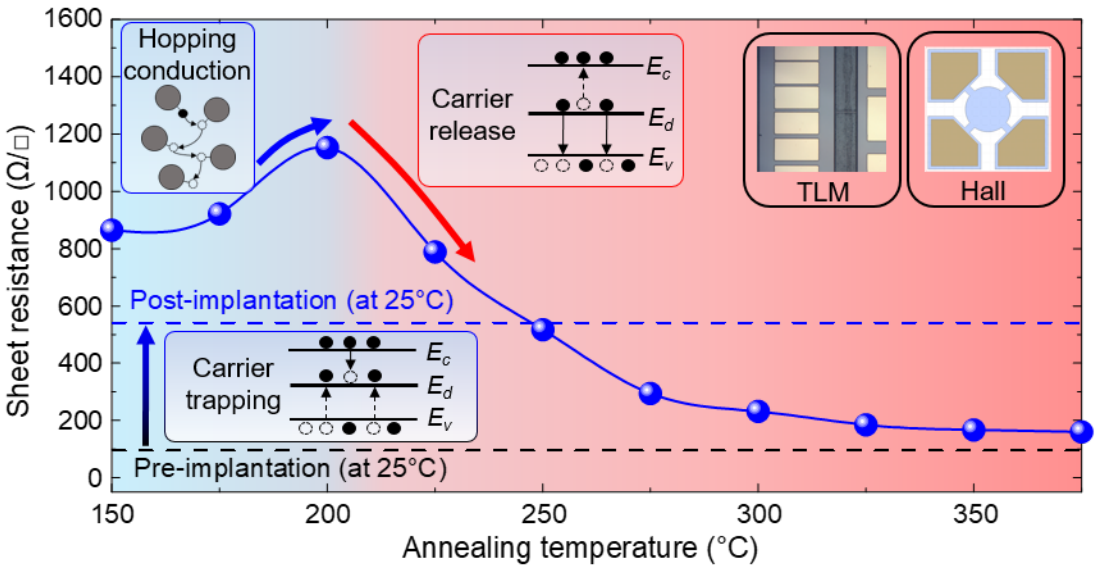

Fig. 4. Average sheet resistance of the implanted *p*-GaSb layer as a function of annealing temperature for the optimal energy and dose combination-C.

It is observed that the sheet resistance goes through a maximum and then falls off. The initial sheet resistance of the *p*-GaSb layer before implant isolation is 102 Ω/□. During implantation, protons interact with the host lattice atoms and give rise to a variety of damage in the form of point defects, defect complexes, and extended defects such as nanovoids and platelets depending upon the implantation parameters. There is an increase of sheet resistance to 547 Ω/□ immediately after

implantation, caused by the trapping of free carriers by deep-level centers created by implantation damage as well as possible carrier mobility degradation by the damage. This carrier trapping and removal occurs along the ion paths. At the optimal dose of ~10^{13} cm^{-2}, almost all charge carriers are trapped, but they can "hop" from one damage site to another. Because of this hopping conduction effect, the post-implantation value of sheet resistance is not the maximum achievable, and subsequent annealing increases the resistivity further.

The evolution of sheet resistance with annealing temperature is typical of a damage-induced compensation scheme. The sheet resistance reaches a maximum of 1153 Ω/ at a temperature of 200°C as damage is annealed out and hopping conduction is reduced: the density of damage sites falls and the probability of trapped carriers to hop from one site to another decreases. In isolation studies of material systems like InP, peak sheet resistance usually increases by orders of magnitude from the post-implantation value; however, this was only ~2 times in our study. This is believed to be the result of GaSb being a low-bandgap material, making it easier for trapped carriers to be thermally excited away from deep-level centers. GaSb also become porous after implantation, which introduces further complexity. Additional annealing eventually reduces the sheet resistance towards the pre-implantation value as captured charge carriers are released, i.e., holes in *p*-GaSb are returned to the valence band from deep-level centers by thermal relaxation. Defect density is also reduced below that required to compensate the material.

In conclusion, an optimized proton implantation scheme was used in conjunction with annealing to increase the electrical resistivity of *p*-GaSb by more than an order of magnitude while introducing no additional optical absorption. This isolation implant step is one of the few important fabrication steps in the direction of realizing GaSb-based monolithic PICs at MWIR wavelengths. Although further work is necessary to identify the types and energy levels of defects produced in proton-implanted *p*-GaSb and eventually in getting even much higher sheet resistance for the targeted applications, the results obtained from this study are still useful for improving knowledge in the low-bandgap material system.

Acknowledgments

This work was supported by the National Science Foundation (NSF) under Grant #2144375.

This work was performed, in part, at the Center for Integrated Nanotechnologies, an Office of Science User Facility operated for the U.S. Department of Energy (DOE) Office of Science. Sandia National Laboratories is a multimission laboratory managed and operated by National Technology & Engineering Solutions of Sandia, LLC, a wholly owned subsidiary of Honeywell International, Inc., for the U.S. DOE's National Nuclear Security Administration under contract DE-NA-0003525. The views expressed in the article do not necessarily represent the views of the U.S. DOE or the United States Government.

The authors would like to thank Chennupati Jagadish, Hoe Tan, and Boon S. Ooi for fruitful discussions.

References

[1] I. E. Gordon, L. S. Rothman, C. Hill, R. V. Kochanov, Y. Tan, P. F. Bernath, M. Birk, V. Boudon, A. Campargue, K. V. Chance, B. J. Drouin, J. M. Flaud, R. R. Gamache, J. T. Hodges, D. Jacquemart, V. I. Perevalov, A. Perrin, K. P. Shine, M. A. H. Smith, J. Tennyson, G. C. Toon, H. Tran, V. G. Tyuterev, A. Barbe, A. G. Császár, V. M. Devi, T. Furtenbacher, J. J. Harrison, J. M. Hartmann, A. Jolly, T. J. Johnson, T. Karman, I. Kleiner, A. A. Kyuberis, J. Loos, O. M. Lyulin, S. T. Massie, S. N. Mikhailenko, N. Moazzen-Ahmadi, H. S. P. Müller, O. V. Naumenko, A. V. Nikitin, O. L. Polyansky, M. Rey, M. Rotger, S. W. Sharpe, K. Sung, E. Starikova, S. A. Tashkun, J. V. Auwera, G. Wagner, J. Wilzewski, P. Wcisło, S. Yu, and E. J. Zak, "The HITRAN2016 molecular spectroscopic database," *Journal of Quantitative Spectroscopy and Radiative Transfer* **203**, p. 3-69 (2017).

[2] M. A. Darwich, A. Shahen, A. Daoud, A. Lahia, J. Diab, and E. Ismaiel, "Non-Invasive IR-Based Measurement of Human Blood Glucose," *Engineering Proceedings* **35**, 1 (2023).

[3] D. M. Tratt, S. J. Young, J. A. Hackwell, D. J. Rudy, D. W. Warren, A. G. Vore, and P. D. Johnson, "MAHI: An Airborne Mid-Infrared Imaging Spectrometer for Industrial Emissions Monitoring," *IEEE Transactions on Geoscience and Remote Sensing* **55**, 8 (2017).

[4] A. Elkhazraji, M. K. Shakfa, N. Abualsaud, M. Mhanna, M. Sy, M. Marangoni, and A. Farooq, "Laser-based sensing in the long-wavelength mid-infrared: chemical kinetics and environmental monitoring applications," *Applied Optics* **62**, 6 (2023).

[5] C. Peng, C. Yang, H. Zhao, L. Liang, C. Zheng, C. Chen, L. Qin, and H. Tang, "Optical Waveguide Refractive Index Sensor for Biochemical Sensing," *Applied Sciences* **13**, 6 (2023).

[6] M. S. I. Sumon, S. Sankar, W. You, I. I. Faruque, S. Dwivedi, and S. Arafin, "Design of GaSb-based monolithic passive photonic devices at wavelengths above 2 μm," *Journal of Physics: Photonics* **5**, 3 (2023).

[7] A. Spott, E. J. Stanton, A. Torres, M. L. Davenport, C. L. Canedy, I. Vurgaftman, M. Kim, C. S. Kim, C. D. Merritt, W. W. Bewley, J. R. Meyer, and J. E. Bowers, "Interband cascade laser on silicon," *Optica* **5**, 8 (2018).

[8] J. R. Meyer, W. W. Bewley, C. L. Canedy, C. S. Kim, M. Kim, C. D. Merritt, and I. Vurgaftman, "The Interband Cascade Laser," *Photonics* **7**, 3 (2020).

[9] Y. Zou, S. Chakravarty, C.-J. Chung, X. Xu, and R. T. Chen, "Mid-infrared silicon photonic waveguides and devices [Invited]," *Photonics Research* **6**, 4 (2018).

[10] S. J. Pearton, “Ion implantation doping and isolation of III–V semiconductors,” *Nuclear Instruments and Methods in Physics Research Section B: Beam Interactions with Materials and Atoms* **59-60**, p. 970 (1991).

[11] U. Schwalke, “Progress in device isolation technology,” *Microelectronics Reliability* **41**, 4 (2001).

[12] J. C. Dyment, J. C. North, and L. A. D'Asaro, “Optical and electrical properties of proton-bombarded p-type GaAs,” *Journal of Applied Physics* **44**, 1 (1973).

[13] S. J. Pearton, C. R. Abernathy, M. B. Panish, R. A. Hamm, and L. M. Lunardi, “Implant-induced high-resistivity regions in InP and InGaAs,” *Journal of Applied Physics* **66**, 2 (1989).

[14] G. D. Henshall, G. H. B. Thompson, J. E. A. Whiteaway, P. R. Selway, and M. Broomfield, "Deep proton-isolated lasers and proton range data for InP and GaSb," *IEE Journal on Solid-State and Electron Devices* **3**, 1 (1979).

[15] J. P. Donnelly, and C. E. Hurwitz, “Proton bombardment in InP,” *Solid-State Electronics* **20**, 8 (1977).

[16] P. Too, S. Ahmed, B. J. Sealy, and R. Gwilliam, "Comparison of two different isolation schemes for n-type InP by helium implantation." *The 10th IEEE International Symposium on Electron Devices for Microwave and Optoelectronic Applications,* p. 160 (2002).

[17] P. Too, S. Ahmed, R. Gwilliam, and B. J. Sealy, "Implant isolation of InP and InGaAs by proton irradiation at variable doses and substrate temperatures." *2001 International Symposium on Electron Devices for Microwave and Optoelectronic Applications. EDMO 2001 (Cat. No. 01TH8567)* (2001).

[18] E. Garmire, H. Stoll, A. Yariv, and R. G. Hunsperger, “Optical waveguiding in proton-implanted GaAs,” *Applied Physics Letters* **21**, 3 (1972).

[19] S. M. Spitzer, and J. C. North, “Electrical and optical properties of proton-bombarded gallium phosphide,” *Journal of Applied Physics* **44**, 1 (1973).

[20] S. J. Pearton, A. R. Von Neida, J. M. Brown, K. T. Short, L. J. Oster, and U. K. Chakrabarti, “Ion implantation damage and annealing in InAs, GaSb, and GaP,” *Journal of Applied Physics* **64**, 2 (1988).

[21] I. Sandall, C. H. Tan, A. Smith, and R. Gwilliam, “Planar InAs photodiodes fabricated using He ion implantation,” *Optics Express* **20**, 8 (2012).

[22] A. G. Milnes, X. Li, A. Y. Polyakov, N. B. Smirnov, A. V. Govorkov, O. M. Borodina, I. V. Tunitskaya, E. A. Kozhukhova, and A. G. Mil'vidskaya, “Ion implantation effects in GaSb,” *Materials Science and Engineering: B* **27**, 2 (1994).

[23] S. Iyer, R. Parakkat, B. Mangalam, B. Patnaik, M. Falvo, and N. Parikh, “A study of the ion implantation damage and annealing behavior in GaSb,” *Journal of Electronic Materials* **25**, 1 (1996).

[24] R. K. Pandey, P. Mishra, J. K. Kaushik, A. Pandey, R. Raman, K. D. Devi, and S. Rath, “Higher electrical activation of ion-implanted Si over S in GaSb epitaxial layers,” *Materials Science in Semiconductor Processing* **115**, 105107 (2020).

[25] R. K. Pandey, P. Mishra, A. Pandey, S. Kumar, A. Goel, and S. Rath, “Effects of Si ion implantation on the surface and electrical characteristics of epitaxial GaSb,” *Vacuum* **198**, 110883 (2022).

[26] S. G. Kim, H. Asahi, M. Seta, J. Takizawa, S. Emura, R. K. Soni, S. Gonda, and H. Tanoue, “Raman scattering study of the recovery process in Ga ion implanted GaSb,” *Journal of Applied Physics* **74**, 1 (1993).

[27] R. Callec, P. N. Favennec, M. Salvi, H. L’Haridon, and M. Gauneau, “Anomalous behavior of ion-implanted GaSb,” *Applied Physics Letters* **59**, 15 (1991).

[28] N. Nitta, M. Taniwaki, Y. Hayashi, and T. Yoshiie, “Formation of cellular defect structure on GaSb ion-implanted at low temperature,” *Journal of Applied Physics* **92**, 4 (2002).

[29] P. Kluth, S. M. Kluth, B. Johannessen, C. J. Glover, G. J. Foran, and M. C. Ridgway, “Extended x-ray absorption fine structure study of porous GaSb formed by ion implantation,” *Journal of Applied Physics* **110**, 11 (2011).

[30] C. D. Merritt, C. S. Kim, M. Kim, C. L. Canedy, W. W. Bewley, M. V. Warren, I. Vurgaftman, and J. R. Meyer, "Effects of ion bombardment on interband cascade laser structures." *Quantum Sensing and Nano Electronics and Photonics XVII* **11288**, p. 215 (2020).

[31] A. Dehzangi, D. Wu, R. McClintock, J. Li, and M. Razeghi, "Planar nBn type-II superlattice mid-wavelength infrared photodetectors using zinc ion-implantation," *Applied Physics Letters* **116**, 22 (2020).

[32] J. F. Ziegler, and J. P. Biersack, "The Stopping and Range of Ions in Matter," *Treatise on Heavy-Ion Science: Volume 6: Astrophysics, Chemistry, and Condensed Matter*, D. A. Bromley, p. 93-129, Boston, MA: Springer US (1985).